*Microscopy and Microanalysis* (2019), 1–11
doi:10.1017/S1431927619000436

Microscopy AND Microanalysis

**Original Article**

# Quantitative Measurement of Iron-Silicides by EPMA Using the Fe L$\alpha$ and L$\beta$ X-ray Lines: A New Twist to an Old Approach

Aurélien Moy[1]*, John Fournelle[1] and Anette von der Handt[2]

[1]Department of Geoscience, University of Wisconsin, Madison, WI 53706, USA and [2]Department of Earth Sciences, University of Minnesota, Minneapolis, MN 55455, USA

**Abstract**

The recent availability of Schottky-type field emission electron microprobes provides incentive to consider analyzing micrometer-sized features. Yet, to quantify sub-micrometer-sized features, the electron interaction volume must be reduced by decreasing accelerating voltage. However, the K lines of the transition elements (e.g., Fe) then cannot be excited, and the L lines must be used. The Fe L$\alpha_{1,2}$ line is the most intense of the L series but bonding effects change its atomic parameters because it involves a valence band electron transition. For successful traditional electron probe microanalysis, the mass absorption coefficient (MAC) must be accurately known, but the MAC of Fe L$\alpha_{1,2}$ radiation by Fe atoms varies from one Fe-compound to another and is not well known. We show that the conventional method of measuring the MAC by an electron probe cannot be used in close proximity to absorption edges, making its accurate determination impossible. Fortunately, we demonstrate, using a set of Fe–silicide compounds, that it is possible to derive an accurate calibration curve, for a given accelerating voltage and takeoff angle, which can be used to quantify Fe in Fe–silicide compounds. The calibration curve can be applied to any spectrometer without calibration and gives accurate quantification results.

**Key words:** EPMA, iron silicide, low kV, MAC, soft X-ray

(Received 5 October 2018; revised 8 January 2019; accepted 14 March 2019)

## Introduction

Natural iron silicide materials have been found in various, generally extremely reducing, environments, e.g., in lightning-induced fulgurites (Essene & Fisher, 1986), in micro-meteoritic impact-formed lunar regolith (Gopon et al., 2013), in rocks formed deep in the Earth's mantle (Shiryaev et al., 2011), and in Project Stardust samples (Rietmeijer et al., 2008). Their study is of great importance to understand the formation mechanism of the materials in which they occur. The size of the natural iron silicide phases can be relatively small (from a few micrometers to tens of nanometers), making their quantification difficult by electron probe microanalysis (EPMA) (Gopon et al., 2013).

Here, we refer to "traditional" EPMA as operation with an accelerating voltage of 15–20 kV or higher, and additionally utilizing the original equipment manufacturer (OEM) or third-party matrix correction software, using the associated published mass absorption coefficients (MACs).

The appearance of the field emission gun, with Schottky sources, in the EPMA realm over the last decade allows the reduction of the electron beam size to few tens of nanometers, enabling sub-micrometer resolution imaging. However, the X-ray lateral spatial analytical resolution remains too large to probe micrometer- and sub-micrometer-sized phases at traditional accelerating voltages, e.g., 15 or 20 kV (for examples of X-ray interaction volume as a function of the material and accelerating voltage, see McSwiggen, 2014; Goldstein et al., 2018). To achieve a smaller analytical spatial resolution, the accelerating voltage needs to be dropped below 10 kV and very likely to 5 or 7 kV. This reduces the electron interaction volume from typically ~1–2 $\mu$m at 15 kV to only ~0.3–0.7 $\mu$m depending on the sample composition and on the X-ray lines used.

However, the main K$\alpha$ X-ray lines of some important elements of the periodic table (typically $Z \geq 25$ at 7 kV and $Z \geq 22$ at 5 kV) can no longer be excited at such low accelerating voltages and the L X-ray lines for these elements must be used for quantification instead. Complications arise for these lines, such as for the transition elements, because complex chemical and physical—mainly crystallographic—effects occur.

Specifically, the L$\alpha_{1,2}$ and L$\beta$ X-ray lines of the transition elements are produced by the transition of an electron from the partially filled outer 3*d* electron shell to an inner electron shell ($L_3$ and $L_2$, respectively). This outer shell is affected by bonding effects due to neighboring atoms. The bonding effects modify the state of these outer electronic shells, which thus modify the associated electron energies and transition probabilities. As a consequence, the different atomic parameters, such as the MAC, the fluorescence yield, the Coster–Kronig, and the super-Coster–Kronig factors, not only depend on the specific element but also on the composition and nature of the material (i.e., crystallography). This implies that the unknown and the standard used for the quantification may have different atomic parameter values for the same element, resulting in matrix correction inaccuracies.

*Author for correspondence: Aurélien Moy, E-mail: amoy6@wisc.edu

Cite this article: Moy A, Fournelle J, von der Handt A (2019) Quantitative Measurement of Iron-Silicides by EPMA Using the Fe L$\alpha$ and L$\beta$ X-ray Lines: A New Twist to an Old Approach. *Microsc Microanal*. doi:10.1017/S1431927619000436

This difficulty led Gopon et al. (2013) to successfully demonstrate the usefulness of the Fe Ll X-ray line to quantify Fe in Fe–silicide samples. This X-ray line has none of the complications of the Fe L$\alpha$ lines, as the Fe Ll involves only core–shell electrons and is far from the associated absorption edge and thus has one well-defined MAC. While this is a useful alternative approach, there remains the issue of the low intensities of Fe Ll X-ray line, which is ~6 times weaker than the Fe L$\alpha_{1,2}$ X-ray line in pure Fe, as seen in Figure 1. The low intensity of the Ll line makes its use difficult for quantification, especially for samples containing <15 wt% of Fe.

This reason has led several authors to reexamine the atomic parameters of the high-count rate L$\alpha_{1,2}$ and L$\beta_1$ X-ray lines for the transition metals, and reevaluate their MACs for use in quantitative EPMA (Llovet et al., 2016; Pinard, 2016; Buse & Kearns, 2018).

To the best of the authors' knowledge, no previous wavelength-dispersive spectrometer (WDS) study has been performed on the use of the combined integrated Fe L$\alpha_{1,2}$ and Fe L$\beta_1$ X-ray lines (i.e., wavescans) to quantify Fe–silicide compounds. This has led us to further examine the high-count rate Fe L$\alpha_{1,2}$ X-ray line for quantitative EPMA. In the following text, the main L X-ray lines, i.e., the Fe L$\alpha_{1,2}$ and the Fe L$\beta_1$ X-ray lines, will simply be denoted Fe L$\alpha$ and Fe L$\beta$, respectively, for the sake of clarity.

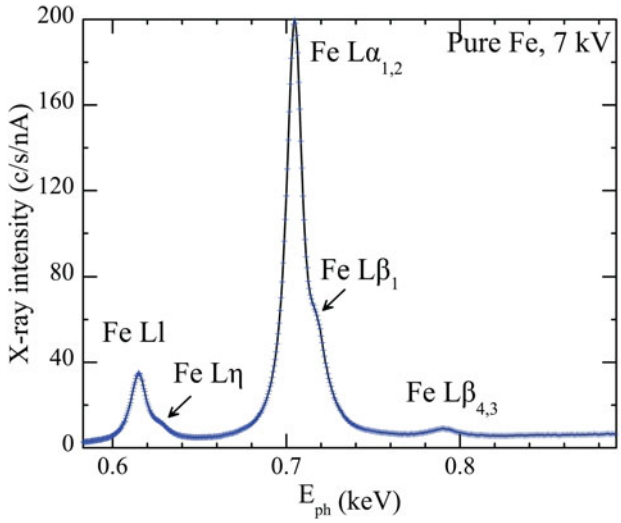


**Figure 1.** Spectrum showing the Fe L X-ray line family recorded on pure Fe at 7 kV and 90 nA using a PC0 (2$d$ spacing of 47.065 Å) monochromator crystal on a CAMECA SXFive FE instrument. The Fe Ll X-ray line is ~6 times less intense than the Fe L$\alpha$ X-ray line.

## Materials and Methods

The current work focuses on the study of 10 bulk synthetic iron silicide compounds with Fe concentrations ranging from 33.6 to 88.88 wt%, and one bulk Fe–metal standard. These samples came from a variety of sources: Philip Gopon synthesized some in the UW Chemistry Department (assisted by Veronica Berns, Rie Fredrickson, and Daniel Fredrickson) by arc melting at 900°C, Ridwan Sakidja and John Perepezko prepared some at the University of Wisconsin-Madison, Department of Material Science & Engineering by arc melting, and others were provided by E. Heikinheimo (Aalto University, Espoo, Finland) and John Spratt (London Museum of Natural History EPMA lab). The Fe–Si phase diagram shows no phases in the Fe range between 0 and 49.9 wt% Fe and between 49.9 and 65.6 wt% Fe. To provide more data points, John Perepezko of the Department of Material Science, University of Wisconsin-Madison, created two samples—$Fe_{33.2}Si_{66.8}$ and $Fe_{57}Si_{43}$ (wt%) by a melt spinning process (Perepezko & Hebert, 2002). As shown in Figure 2, these samples are not perfectly homogeneous and present several phases, but they become smaller as we approach the edge of the sample. At a distance of about 2 $\mu$m from the rim, the phases are small enough to consider the sample homogeneous, relative to the size of the electron interaction volume.

The composition of each sample was measured by EPMA at the Eugene Cameron Electron Microprobe Laboratory, Department of Geoscience, University of Wisconsin-Madison, using a CAMECA SXFive FE microprobe (CAMECA, Paris, France), at 10, 15, and 20 kV, with a beam current of 20 nA. The element Fe was analyzed using the K$\alpha$ X-ray line with two LiF crystals (interplanar spacing $2d = 4.0267$ Å), and the element Si was analyzed using the K$\alpha$ X-ray line with two LPET crystals ($2d = 8.750$ Å). Five measurements were acquired and averaged for each accelerating voltage and each sample. High purity metallic Fe and pure Si elements were used as reference materials. All the samples, as well as the standards, were C-coated at the same time to ensure electrical conductivity. The coating thickness was

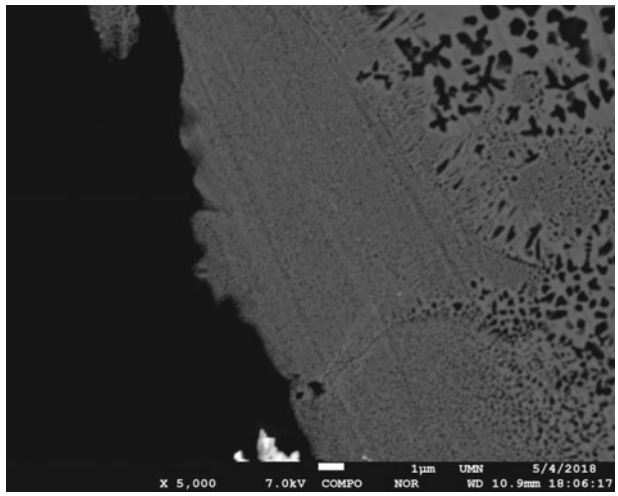


**Figure 2.** Backscattered electron image of the $Fe_{20}Si_{80}$ sample obtained by the spin glass method (Perepezko & Hebert, 2002) and used in this study. The image was acquired at 7 kV and 17 nA. The core of the sample presents two mixed micrometer-wide phases. The size of the phases decreases toward the edge and reaches a nanometer scale.

determined by measuring the C K$\alpha$ $k$-ratio on the 10 samples and on an HOPG graphite standard at 10, 15, 20, and 25 kV with the LPC2 diffractor ($2d = 99.136$ Å). Thin film software STRATAGem (Version 2.6) was used to determine the carbon coat thickness utilizing the PAP matrix correction algorithm (Pouchou & Pichoir, 1991). An average carbon thickness of 16.6 nm was found (using a traditional density of 2.2 g/cm$^3$ for carbon), with a standard deviation of 1.8% between all the samples. "Probe for EPMA" software (Donovan et al., 2018) with the PAP matrix correction and the MAC30 mass absorption coefficients (Heinrich, 1987) were used to acquire the data and perform the quantification. The composition of the samples is shown in Table 1.

An initial attempt was made to quantify the samples using the CAMECA SXFive FE electron probe using the Fe L$\alpha$ X-ray peak

**Table 1.** Composition of the Iron Silicide Samples Used in This Study, Measured at 10, 15, and 20 kV.

| Sample Name | Elemental wt% | 10 kV | 15 kV | 20 kV | Average | RSD % |
|---|---|---|---|---|---|---|
| S4 | Fe | 88.70 | 88.98 | 88.95 | 88.88 | 0.77 |
| | Si | 11.28 | 11.13 | 11.10 | 11.17 | 0.39 |
| | Total | | | | 100.05 | 0.68 |
| S6t | Fe | 87.22 | 87.15 | 87.36 | 87.25 | 0.90 |
| | Si | 13.72 | 13.53 | 13.55 | 13.60 | 0.50 |
| | Total | | | | 100.85 | 0.78 |
| S5 | Fe | 86.85 | 87.05 | 87.56 | 87.16 | 0.63 |
| | Si | 12.52 | 12.30 | 12.27 | 12.36 | 0.47 |
| | Total | | | | 99.52 | 0.55 |
| 94-1 bot | Fe | 83.79 | 82.73 | 83.06 | 83.19 | 0.47 |
| | Si | 16.89 | 16.85 | 16.60 | 16.78 | 0.50 |
| | Total | | | | 99.97 | 0.40 |
| 94-1 top m | Fe | 68.27 | 67.63 | 67.87 | 67.93 | 0.60 |
| | Si | 33.09 | 32.89 | 32.98 | 32.99 | 0.18 |
| | Total | | | | 100.91 | 0.41 |
| Fe40 | Fe | 57.88 | 56.98 | 57.23 | 57.36 | 0.82 |
| | Si | 43.12 | 43.13 | 43.03 | 43.09 | 0.51 |
| | Total | | | | 100.46 | 0.52 |
| S3b | Fe | 51.20 | 50.88 | 50.91 | 51.00 | 0.69 |
| | Si | 49.60 | 49.32 | 49.33 | 49.41 | 0.22 |
| | Total | | | | 100.41 | 0.37 |
| S3t | Fe | 51.33 | 50.46 | 50.81 | 50.86 | 0.71 |
| | Si | 49.55 | 49.71 | 49.52 | 49.60 | 0.20 |
| | Total | | | | 100.46 | 0.37 |
| S6b | Fe | 46.36 | 46.02 | 45.94 | 46.11 | 0.36 |
| | Si | 54.46 | 54.01 | 53.80 | 54.09 | 0.13 |
| | Total | | | | 100.20 | 0.18 |
| Fe20 | Fe | 33.49 | 33.77 | 33.56 | 33.60 | 0.86 |
| | Si | 66.11 | 65.88 | 65.90 | 65.96 | 0.30 |
| | Total | | | | 99.56 | 0.35 |

RSD stands for relative standard deviation.

intensity at 7 kV and 90 nA [using a LTAP diffractor crystal ($2d$ = 25.745 Å)] and specifying the Si concentration from the results obtained at 15 kV. The quantification results were obtained using the traditional PAP matrix correction algorithm and MAC30 mass absorption coefficients. Table 2 shows that the Fe concentrations deviate strongly from the expected values; lower Fe concentrations show greater difference between the expected and experimental values. This shows the problematic use of the Fe L$\alpha$ X-ray line with the traditional EPMA quantification method to determine Fe in Fe–silicide samples.

In addition, Fe L$\alpha$ and L$\beta$ X-ray line spectra were recorded on the CAMECA SXFive FE microprobe at 7 kV and 90 nA with three different spectrometers: TAP and LTAP crystals ($2d$ = 25.745 Å) and a PC0 crystal ($2d$ = 47.065 Å). A pulse height analyzer (PHA) was set in differential mode to perform the measurements to be consistent with further measurements performed at higher accelerating voltages, as explained later in this paper.

Equivalent spectra were also acquired at the Department of Earth Sciences, University of Minnesota, using a JEOL JXA-8530F Plus microprobe (JEOL Ltd., Tokyo, Japan) equipped with a new diffraction grating-CCD type spectrometer: a soft X-ray emission spectrometer (SXES). The operating conditions used were 7 kV and 20 nA. This spectrometer acquires the whole spectrum in parallel (versus the traditional Rowland circle WDSs which have to serially scan the range of wavelengths to generate a spectrum) between 0.237 and 2.845 keV (using SXES grating JS2000 with 4,096 parallel channels). Both types of spectrometers used (WDSs and SXES) have a takeoff angle of 40°.

Much time was spent in attempting to determine the correct MACs for the various iron silicides. Eventually it was realized that there were insurmountable obstacles to determining the Fe

**Table 2.** Quantification Results for the Fe Content of the Studied Samples Using the Fe Lα X-ray Line at 7 kV.

| Sample Name | Fe20 | S6b | S3t | S3b | Fe40 | 94-1 top m | 94-1 bot | S5 | S6t | S4 |
|---|---|---|---|---|---|---|---|---|---|---|
| Nominal (Fe wt%) | 33.60 | 46.11 | 50.86 | 51.00 | 57.36 | 67.93 | 83.19 | 87.16 | 87.25 | 88.88 |
| Traditional EPMA (Fe wt%) | 51.89 | 72.02 | 83.68 | 84.01 | 77.80 | 86.74 | 90.53 | 91.79 | 92.92 | 91.80 |
| Rel. err. (%) | 54.4 | 56.2 | 64.5 | 64.7 | 35.6 | 27.7 | 8.8 | 5.3 | 6.5 | 3.3 |

The Si concentration has not been reacquired and data measured in Table 1 were used for the matrix correction.

Lα MACs accurately (see the "Discussion" section) and hence, a different approach was needed. "Going back to the drawing board" led to integration of the Fe Lα and Fe Lβ wavescan peaks together (both background subtracted and then normalized by the same peak integrated value of pure Fe), generating a series of "area Fe Lα–Lβ wavescan *k*-ratios" (subsequently referred to as "area *k*-ratios") which were then plotted against the respective Fe content of the iron silicides. As shown in Figure 3, a simple relationship became evident.

The uncertainties are calculated as follows: for a given spectrum, the statistics of the number of photons recorded in each bin (in counts) follows a Poisson distribution. The uncertainty associated with the measurement will then be given by $\sqrt{N}$, where $N$ is the number of photons recorded in each bin. For a uniform step size, the statistical uncertainty of the area will then be given by

$$\Delta\text{Area} = \sqrt{\sum_{i=1}^{n} N_i} \times \frac{\Delta E}{I \cdot t}$$

where $N_i$ is the number of counts recorded in the bin $i$, $n$ is the number of bins, $\Delta E$ is the step size between two bins in keV, $I$ is the beam current in nA, and $t$ is the dwell time in s. When several spectra are averaged, their respective uncertainties are also added quadratically.

Using this method, the uncertainties on the calculated area were ~0.2%, and up to ~0.3% for the sample with the lowest Fe concentration. The uncertainty on the area *k*-ratio was then, on average, ~0.3%.

## Results

Figure 3 shows the Fe concentration in weight percent (wt%) versus the area *k*-ratio. The data form a smooth trend that can be easily fitted by a third-order polynomial with the limit conditions of the Fe concentration being 0 when the area *k*-ratio is 0 and being as close as possible to 100 wt% when the area *k*-ratio is 1. Only the average of data from samples containing 50.86 and 51.00 wt % of Fe deviates from the trend. Both samples were mounted on the same epoxy mount and we suggest that the deviation is caused by a tilt of the mount changing the takeoff angle (as discussed later), rather than reflect statistical uncertainties or analytical problems. If both these samples are omitted from the fit, the experimental values are almost perfectly represented by the polynomial curve ($R^2 = 0.996$) whose equation is displayed in Figure 3. Using all experimental data, the quality of the fit degrades slightly to an $R^2 = 0.991$ but remains in good agreement with the data.

Notably, the spectrometer with the PC0 diffractor crystal shows a consistent lower area *k*-ratio for a given Fe concentration, compared with the other spectrometers (Fig. 3). This can be due to the background removal method used to determine the peak area. Here, the background was fitted by a linear curve using spectrum positions far from the tail of the peaks. However, the bremsstrahlung is affected by an increase in absorption below the Lα and Lβ peaks because of the absorption edges of the Fe atoms. Thus, fitting the bremsstrahlung with a linear curve can only be an approximation and likely underestimates the peak area. Notably, the spectrometer with the PC0 crystal also has the lowest peak over the background ratio compared with other spectrometers, in line with it showing the largest deviation from the fit. In general, the larger the peak-to-background ratio, the smaller is the error on the calculated area estimate.

We also observe that the SXES spectrometer gives systematically higher area *k*-ratios in most cases. This might be due to an overall tilt of the sample holder slightly changing the takeoff angle between the sample surface and the spectrometer.

Optimally, a separate set of known Fe–Si samples would be evaluated, to apply the calibration curve in order to test its accuracy. However, there is a limited set of samples and they were all used to generate the calibration curve.

Nevertheless, to test the predictions of the calibration curve, we used the best fitting curve (the one excluding the S3t and S3b samples) to reevaluate the Fe concentration of our samples (Table 3). The quantification results are highly improved compared with the traditional method using the Fe Lα X-ray line alone. The highest deviations are obtained, as expected, for samples S3t and S3b with a relative deviation of 8.9% for both samples. Other results always have a relative error smaller than 3.6%.

Spectra measurement and the calculation of the area *k*-ratios have also been performed at 3, 5, 10, 15, 20, 25, and 30 kV with a takeoff angle of 40° using the three WDSs (LTAP, TAP, and PC0 crystals) on the CAMECA SXFive microprobe. During the measurements, the PHA was also set in differential mode to avoid the 9th order of diffraction of the Fe Kα X-ray line at 0.711 keV that can arise when the electron beam energy is higher than the critical ionization energy of the Fe K electron shell ($E_c$ = 7.114 keV). The resulting calibration curves are similar to the calibration curve previously obtained at 7 kV (Figs. 4a, 4b). A good coefficient of determination was obtained by fitting the data with a third-order polynomial function with no constant coefficient. The samples containing 50.86 and 51.00 Fe wt% (S3t and S3b) were excluded from the fit again for the reasons discussed above.

The measurements performed from 3 to 30 kV show a gradual increase of the disparity of *k*-ratio measurements (Fig. 5). This can best be explained by the fact that at increasing accelerating voltages, the emitted X-ray intensities are more sensitive to the takeoff angle. The X-rays are produced deeper in the sample and experience strong absorption by the material. Changes to the X-ray path length caused by small tilts of the sample surfaces relative to each other result in an increase or a decrease of the measured X-ray intensity, depending on the position of the spectrometers relative to the sample surface, and thus increase the standard deviation of the measurements. In addition, for almost

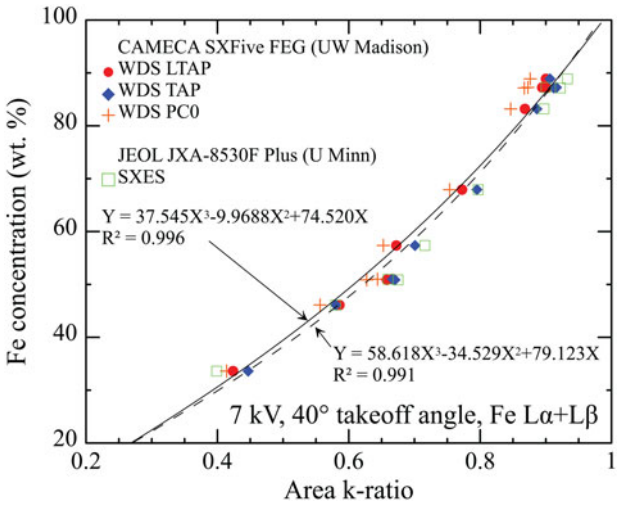


**Figure 3.** Measured area *k*-ratio acquired at 7 kV versus the Fe concentration in iron-silicides. A good agreement is shown between all the spectrometers used. The symbols represent the average value of all the measurements for each spectrometer. The fit of the averaged data including all the samples is represented by the dashed curve while the solid line fit excludes the samples containing 50.86 and 51.00 Fe wt% (for explanation see the text).

all the different accelerating voltages used and for all the different samples studied, the *k*-ratios measured with the spectrometer using the PC0 crystal were systematically lower than the *k*-ratios measured with the spectrometer using the LTAP crystal that were systematically lower than the *k*-ratios measured with the spectrometer using the TAP crystal. This also suggests that the takeoff angle may be different among the spectrometers.

For a given Fe concentration, the *k*-ratio increases with the accelerating voltage from 3 to 10 kV and then decreases from 10 to 30 kV. This is due to the competition between two different processes: the X-ray production that increases as the primary electron energy increases and the attenuation of the emitted X-rays, due to absorption in the material, that also increases as the X-rays are produced deeper in the sample. The maximum X-ray emission seems to be reached around 10 kV, for all the Fe–silicide samples. This behavior of the *k*-ratios correlates with the changes of the fitting polynomial coefficients as a function of the accelerating voltage, as shown in Figure 6. Despite the 3 kV values, the fitting coefficients seem to follow a trend with a strong change around 10 kV. The coefficients rapidly increase before 10 kV and then plateau between 10 and 30 kV. The 3 kV values seem to be anomalous and off the trend and this can be due to the higher degree of statistical fluctuations in the measurements recorded at 3 kV that imply higher uncertainties in the data and thus in the fitting coefficients.

## Discussion

It has been generally accepted over the past several decades that quantitative EPMA, particularly in materials science, is routinely performed using matrix corrections with some versions of a ZAF or phi-rho-*Z* algorithm, with a key component being the MAC. We expected this to be the case in our lead up to this study, and worked to develop a way to utilize the Fe L$\alpha$ X-ray intensities in quantifying iron in iron silicides. After several months of in-depth scrutiny of dozens of spectra, we re-evaluated the initial premise. In the following, we will explore the theoretical basis as to why we believe it is not possible to accurately determine the MAC of the Fe L$\alpha$ and L$\beta$ X-ray lines by Fe atoms, and more generally to determine the MAC of an element close to its absorption edges, using the traditional "EPMA MAC extrapolation" technique as detailed below.

### Theory

The number of characteristic X-rays of energy $E_x$, emitted by an element A and recorded per unit of time, for a given electronic transition, can be described by the so-called fundamental equation of microanalysis (Scott et al., 1995; Fournier et al., 1999):

$$I_X(E_x) = C_A \frac{N_a}{A_r} n_{el} \omega_i^A \Gamma_{ij}^A Q_i^A(E_0) \times \int_0^\infty \varphi_i(\rho z) e^{-(\mu/\rho)(E_x)(\rho z/\sin\theta_d)} d\rho z \, \varepsilon(E_x) \frac{\Delta\Omega}{4\pi} F(1+g_{CK}) \quad (1)$$

where $I_X(E_x)$ represents the number of characteristic X-rays of energy $E_x$ recorded per second, $C_A$ and $A_r$ are the concentration and the atomic mass of the studied element A, respectively. $N_a$ is the Avogadro's number and $n_{el}$ is the number of incident electrons per second. $\omega_i^A$ is the fluorescence yield for element A with a primary ionization in the electron shell $i$ (i.e., the probability to emit a photon during relaxation of atom A with an initial vacancy in the electron shell $i$). $\Gamma_{ij}^A$ is the electron transition rate from electron shell $j$ to $i$ (i.e., the probability that the relaxation occurs by the transition of an electron from the shell $j$ to the vacancy located in shell $i$). $Q_i^A(E_0)$ represents the ionization cross-section of element A, in cm$^2$, of the electron shell $i$ for an incident electron of energy $E_0$. $\varphi_i(\rho z)$ is the so-called phi-rho-$Z$ function that represents the ionization depth distribution, in the material of interest, for the shell $i$ of element A at mass depth $\rho z$, and for an incident electron beam of energy $E_0$. The next term in equation (1), represented by the exponential factor, describes the absorption of the X-rays produced inside the sample before they escape the sample with a takeoff angle $\theta_d$ corresponding to the direction of the spectrometer. $(\mu/\rho)(E_x)$ is the MAC, in cm$^2$/g, of the sample for X-rays of energy $E_x$. $\varepsilon(E_x)$ and $\Delta\Omega/4\pi$ correspond to the intrinsic and geometric detection efficiencies of the spectrometer, respectively. The intrinsic detection efficiency depends on the energy of the recorded photon. $F$ represents the secondary fluorescence enhancement factor ($F \geq 1$) and the factor $(1 + g_{CK})$ represents the enhancement in the production of the characteristic X-rays by Coster–Kronig and super-Coster–Kronig transitions.

This equation is valid in the most common cases, but some simplifications are assumed which may be problematic in certain circumstances. Indeed, in equation (1) the characteristic X-rays produced are supposed to be emitted at an exact energy, the characteristic energy $E_x$, but due to Heisenberg's uncertainty principle between energy and time, the characteristic X-ray line has a natural width (also called natural broadening) that usually follows a Lorentzian shape (for radiative electron transitions between inner electron shells) whose maximum is centered on the characteristic energy $E_x$.

The energy response function of the spectrometer must also be considered. This response function is dependent on the X-ray energy recorded $E_{ph}$. In the case of monochromator crystals, because of defects in the crystal (such as mosaic defects) and because of the finite size of the crystal, the crystal response

**Table 3.** Reevaluation of the Fe Content of the Studied Samples Using the Obtained Calibration Curve.

| Sample Name | Fe20 | S6b | S3t | S3b | Fe40 | 94-1 top m | 94-1 bot | S5 | S6t | S4 |
|---|---|---|---|---|---|---|---|---|---|---|
| Nominal Fe wt% | 33.60 | 46.11 | 50.86 | 51.00 | 57.36 | 67.93 | 83.19 | 87.16 | 87.25 | 88.88 |
| Calibration curve Fe wt% | 32.40 | 46.75 | 55.37 | 55.56 | 58.48 | 69.82 | 82.66 | 86.43 | 85.76 | 86.94 |
| Rel. err. (%) | −3.59 | 1.40 | 8.86 | 8.94 | 1.95 | 2.79 | −0.64 | −0.84 | −1.71 | −2.18 |

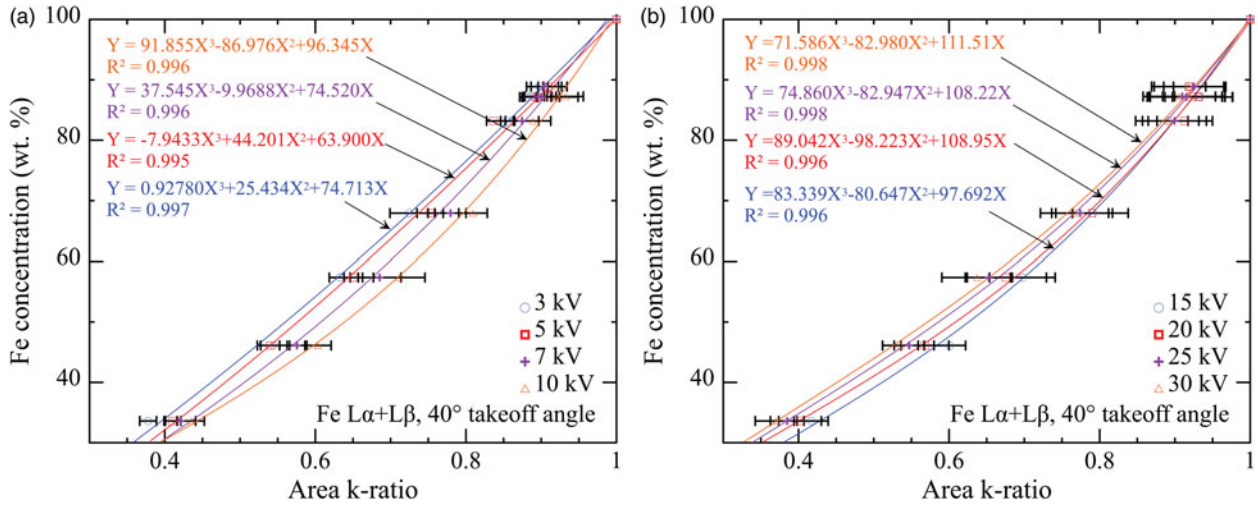


**Figure 4.** Area *k*-ratio calibration curves measured with a takeoff angle of 40° at 3, 5, 7, and 10 kV (**a**) and measured at 15, 20, 25, and 30 kV (**b**). The error bars represent the standard deviation of the three measurements made at each accelerating voltage.

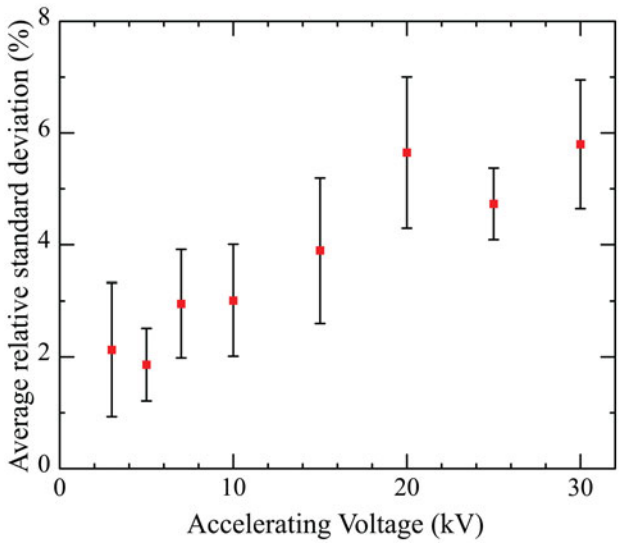


**Figure 5.** Standard deviation of the area *k*-ratio measurements versus the accelerating voltage. Each point corresponds to the average of the standard deviations obtained on each sample for a given accelerating voltage. The data clearly show an increase of the disparity in the measurements with increasing voltage, suggesting the sample surfaces are not perfectly normal to the beam.

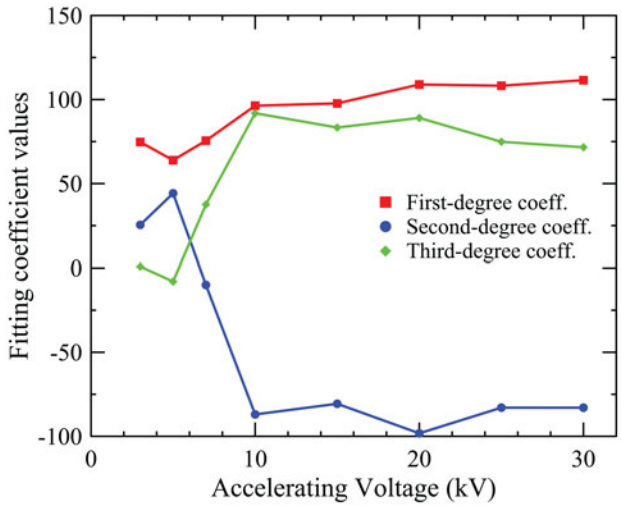


**Figure 6.** Variation of the fitting coefficients given in Figure 4 as a function of the accelerating voltage.

function is not following ideal Bragg's law, which means that not only will the wavelength satisfying $n\lambda = 2d \sin(\theta)$ (where $n$ is the order of diffraction, $\lambda$ is the X-ray wavelength in Å, $2d$ is the interplanar spacing in Å, and $\theta$ is the angle of diffraction) be diffracted, but also the contiguous wavelength of length $\lambda \pm d\lambda$. In an energy representation, photons with an energy $E_{ph} + dE$ will also be diffracted by the crystal, but with a probability that decreases as $|dE|$ increases. The crystal response function can be well described by a Gaussian function centered on the measured energy $E_{ph}$ and characterized by a full width at half maximum $\Gamma_G$, but the following discussion remains valid for other, more realistic, spectrometer response functions. During the measurements of X-rays of energy $E_{ph}$, all the photons in the range $[E_{ph} - 3\Gamma_G; E_{ph} + 3\Gamma_G]$ are appreciably diffracted by the crystal (at the first order of diffraction)

with an intensity following the Gaussian response function. In traditional WDS, the X-rays are usually detected by a gas flow detector or by a sealed gas detector. The response function of the gas detector is usually represented by an integrator and all the photons reaching and interacting with the detector are recorded, without consideration of their energy. An energy window can be used to discriminate against high order X-ray diffraction (corresponding to higher energies) but usually cannot distinguish between photons in an energy range as small as $[E_{ph} - 3\Gamma_G; E_{ph} + 3\Gamma_G]$.

Finally, by considering the natural broadening and the spectrometer broadening, the X-ray intensity recorded at the photon energy $E_{ph}$ is given by:

$$I(E_{ph}) = \int_{-\infty}^{+\infty} I_X(E)\, L(E)\, G(E - E_{ph})\, dE \tag{2}$$

where $I_X(E)$ is the theoretical emitted X-ray intensity [equation (1)], $L(E)$ is the Lorentzian function representing the natural broadening of the characteristic X-ray line, and $G(E)$ is the Gaussian function representing the response function of the spectrometer. Equation (2) represents the convolution product of $I_X(E)\, L(E)$ with $G(E)$. It is worth noting that $L$ is normalized, i.e., the area under the function $L(E)$ is equal to 1.

When $\varepsilon(E_{ph})$ is constant over the energy range $[E_{ph} - 3\Gamma_G; E_{ph} + 3\Gamma_G]$, which is usually the case except for close to the Ar K absorption edge for a P10 gas flow detector or close to the Xe L edges for a sealed Xe gas detector, and when the MAC, $(\mu/\rho)(E_{ph})$, is also constant over the same range of energy, which is the case when there is no absorption edge in close vicinity, $I_X$ is independent of the photon energy $E_{ph}$ and then can be extracted from the previous integral. By normalizing the unknown intensity to a standard intensity, i.e., by calculating the $k$-ratio, and by assuming that (1) the natural broadening of the studied X-ray line is the same for both the unknown and the standard, which is the case for inner shell transitions, and (2) that the spectrometer broadening is the same between the measurements performed on the unknown and on the standard, which is the case when the spectrometer conditions are the same, and (3) if the measurements were acquired in a relative short period of time, the $k$-ratio ($k_r$) can be expressed as:

$$k_r = \frac{I_u(E_{ph})}{I_s(E_{ph})} = \frac{I_X^u \int_{-\infty}^{+\infty} L(E)\, G(E - E_{ph})\, dE}{I_X^s \int_{-\infty}^{+\infty} L(E)\, G(E - E_{ph})\, dE} = \frac{I_X^u}{I_X^s} \tag{3}$$

This is the traditional expression of the $k$-ratio used in microanalysis. It is worth noting that, for a single electron transition (i.e., for a single characteristic X-ray line), the convolution $\int_{-\infty}^{+\infty} L(E)\, G(E - E_{ph})\, dE$ is the well-known Voigt function used to describe the shape of the recorded X-ray lines (Ida et al., 2000; Rémond et al., 2002).

## MAC Calculation Difficulties

However, in the case of the Fe L$\alpha$ and Fe L$\beta$ X-ray lines, because of the proximity to the $L_3$ and $L_2$ absorption edges, the MAC is not constant over the energy range $[E_{ph}\text{-}3\Gamma_G; E_{ph} + 3\Gamma_G]$, and thus $I_X(E)$ depends on the photon energy and cannot be extracted from the convolution product. The measured $k$-ratio will then depend on the spectrometer broadening, i.e., on the specific instrument used and hence will not be suitable for deriving a true, universally applicable MAC.

Fortunately, by integrating the X-ray intensity over the entire energy spectrum, theoretically from $-\infty$ to $+\infty$ but practically from and to integration bounds where the convolution product of $I_X(E)L(E)$ by $G(E)$ is almost equal to zero, i.e., from $E_{ph} - 3\Gamma_G - 3\Gamma_L$ to $E_{ph} + 3\Gamma_G + 3\Gamma_L$, the integral of the convolution product can be separated into the product of two integrals:

$$\int_{-\infty}^{+\infty}\int_{-\infty}^{+\infty} I_X(E)\, L(E)\, G(E - E_{ph}) dE dE_{ph} = \int_{-\infty}^{+\infty} I_X(E)\, L(E)\, dE \int_{-\infty}^{+\infty} G(E)\, dE \tag{4}$$

By calculating the $k$-ratios using the area of the X-ray lines, we obtain:

$$k_{r,Area} = \frac{\int_{-\infty}^{+\infty} I_X^u(E) L_u(E)\, dE \int_{-\infty}^{+\infty} G(E)\, dE}{\int_{-\infty}^{+\infty} I_X^s(E) L_s(E)\, dE \int_{-\infty}^{+\infty} G(E)\, dE} = \frac{\int_{-\infty}^{+\infty} I_X^u(E)\, L_u(E)\, dE}{\int_{-\infty}^{+\infty} I_X^s(E) L_s(E)\, dE} \tag{5}$$

This shows the area $k$-ratio is independent of the spectrometer broadening and so is suitable for the acquisition of a universal calibration curve. In case of overlaps between several characteristic X-ray lines, equation (5) simply becomes:

$$k_{r,Area} = \frac{\int_{-\infty}^{+\infty} \sum_l I_{X,l}^u(E) L_{u,l}(E)\, dE}{\int_{-\infty}^{+\infty} \sum_l I_{X,l}^s(E) L_{s,l}(E)\, dE} \tag{6}$$

where the indices $l$ represents the overlapping X-ray lines.

The method presented by Pouchou and Pichoir (Pouchou & Pichoir, 1988; Pouchou, 1996) to experimentally measure the MAC for an X-ray line of energy $E_{ph}$ for a given element, using an electron microprobe, consists of the measurement of the X-ray intensity at the energy $E_{ph}$ of a characteristic X-ray line at several accelerating voltages. Note: this method ("XMAC") required measurements at a single spectral position, typically the peak maximum. The acquired curve representing the measured X-ray intensity versus the accelerating voltage is then normalized by the intensity measured at one voltage, usually 5 or 7 kV. The normalized curve is then fitted using equation (3), where $I_s(E_{ph})$ has been replaced by the normalizing intensity (measured on the unknown), and in which the MAC is set as the fitting parameter. It is worth mentioning that this method is dependent on the phi-rho-$Z$ model used and that different models may give different, but close, MAC values. By using the PAP, or XPP (Pouchou, 1996), model, "a good agreement with the most recent tabulated values is obtained in various systems where the energy of the emission line is not too close to an absorption edge" (Pouchou & Pichoir, 1988). Indeed, in the vicinity of the absorption edges "very strong deviations occur for the lighter metals (Ni to Sc)" (Pouchou & Pichoir, 1988) compared with tabulated data.

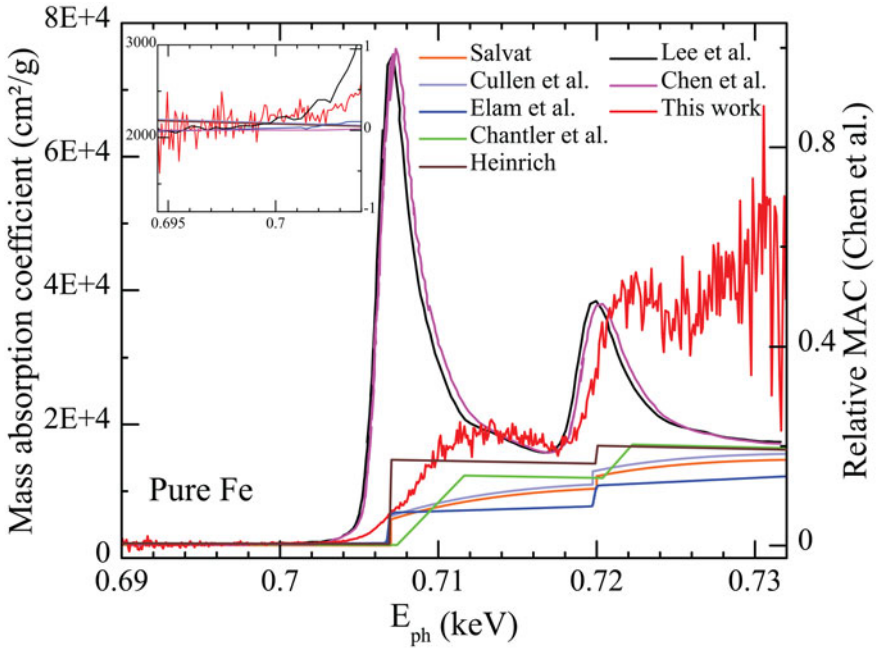


**Figure 7.** Experimental (Chen et al., 1995; Lee et al., 2009) and theoretical (Heinrich, 1987; Cullen et al., 1997; Elam et al., 2002; Chantler et al., 2005; Salvat, 2015) MACs of pure Fe for X-ray energies ranging from 0.690 to 0.732 keV. The inset shows the good agreement obtained between the described method and other experimental and theoretical data far from the absorption edge.

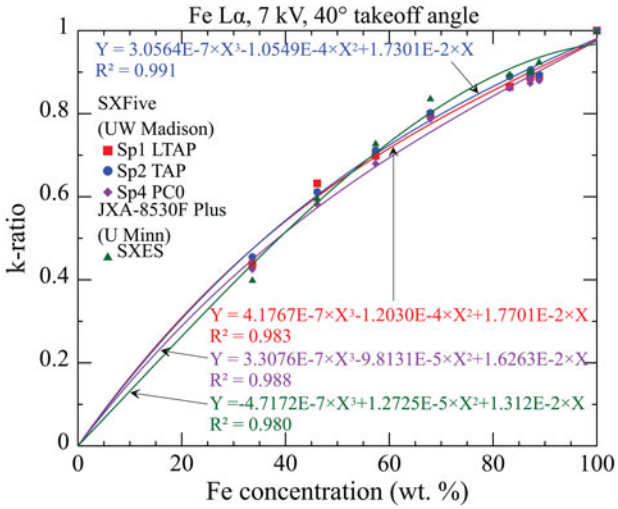


**Figure 8.** Calibration curves obtained by measuring the maximum net peak intensity of the Fe L$\alpha$ X-ray line acquired with three monochromator crystals and with the SXES. The curves obtained for the LTAP and TAP crystals are very similar as their instrumental broadening are also similar.

As explained earlier, as the intensity $I_X$ ($E_{ph}$) depends on the photon's energy because of the MAC, the acquired value, in addition to being incorrect, will be dependent on the spectrometer response function and thus measuring it on different instruments will give different results.

However, fortunately two research groups have measured Fe L$\alpha$ MACs directly, using very intense X-rays generated in synchrotrons: Chen et al. (1995) and Lee et al. (2009). These will be referred to in the following paragraphs. Sokaras et al. (2011) also measured the Fe L$\alpha$ MACs using synchrotron radiation but due to the lack of experimental details (especially the resolving power) and due to the disagreement of these data with the two other sets of experimental data between the absorption edges, Sokaras et al.'s data were not included in the following discussion—although their data agree well far from the absorption edges.

To illustrate further the problem with determining MACs by EPMA, we have applied the Pouchou and Pichoir's method on pure Fe to reevaluate the Fe L$\alpha$ and Fe L$\beta$ X-ray MAC by atoms of Fe. This new method was applied to all 512 photon energy channels ranging from 0.686 to 0.733 keV, each one leading to a different MAC value. The measurements were performed using the CAMECA SXFive FE microprobe at 2.5, 3, 5, 7, 10, 15, 20, 25, and 30 kV and 90 nA using a wavelength dispersive spectrometer equipped with a LTAP monochromator crystal. The resulting MAC curve, as a function of the photon energy, was compared with experimental MACs measured on synchrotron beamlines (Chen et al., 1995; Lee et al., 2009) and with widely used theoretical MACs extracted from the MAC30 (Heinrich, 1987), EPDL97 (Cullen et al., 1997; Elam et al., 2002), FFAST (Chantler et al., 2005), and PENELOPE 2014 (Salvat, 2015) databases, as shown in Figure 7.

The measurements performed by Chen et al. (1995), given in relative units, were rescaled to match the values measured by Lee et al. (2009) at 0.695 and 0.735 keV. The Lee et al. (2009) data were acquired at the Lawrence Berkeley National Laboratory Advanced Light Source beamline 6.3.1. The incident X-ray energy was varied using a variable line spacing plane grating monochromator that has a resolving power $E/\Delta E =$ 3,000, an order of magnitude better than the resolving power of the spectrometers used on the electron microprobe. The data were measured using the electron yield method.

The theoretical MACs are not known to be accurate close to the absorption edges, but they provide reliable values away from

**Table 4.** Reevaluation of the Fe Concentration of the Fe–Si Samples Using the "Non-Universal" Calibration Curves, Each Spectrometer Having its Own Curve.

| Sample Name | Fe20 | S6b | Fe40 | 94-1 top m | 94-1 bot | S5 | S6t | S4 |
|---|---|---|---|---|---|---|---|---|
| Nominal Fe wt% | 33.60 | 46.11 | 57.36 | 67.93 | 83.19 | 87.16 | 87.25 | 88.88 |
| Sp1 calibration curve (Fe wt%) | 30.60 | 50.19 | 58.18 | 71.84 | 81.92 | 85.46 | 86.79 | 85.94 |
| Rel. err. (%) | 8.94 | −8.84 | −1.42 | −5.76 | 1.53 | 1.95 | 0.52 | 3.31 |
| Sp2 calibration curve (Fe wt%) | 33.21 | 48.71 | 60.32 | 72.16 | 85.07 | 86.20 | 87.47 | 85.51 |
| Rel. err. (%) | 1.18 | −5.64 | −5.16 | −6.24 | −2.25 | 1.10 | −0.25 | 3.78 |
| Sp4 calibration curve (Fe wt%) | 31.73 | 47.36 | 58.67 | 72.62 | 83.03 | 84.83 | 86.17 | 85.68 |
| Rel. err. (%) | 5.59 | −2.72 | −2.27 | −6.91 | 0.19 | 2.67 | 1.23 | 3.60 |
| SXES calibration curve (Fe wt%) | 30.75 | 47.37 | 60.41 | 73.71 | 83.78 | 85.26 | 84.64 | 91.20 |
| Rel. err. (%) | 8.51 | −2.74 | −5.32 | −8.52 | −0.71 | 2.18 | 2.98 | −2.62 |

those edges. The error associated with the traditional theoretical MACs is usually estimated to be better than 10% in the range 100 eV to 1 keV (Cullen et al., 1997). The various theoretical MACs are using different photoionization subshell binding energies, causing an energy shift of the absorption edges between the different evaluations. For the sake of consistency, the EPDL97 and PENELOPE 2014 data were shifted by −13.8 and −6 eV, respectively, to match the Elam et al. (2002) data.

For X-ray energies lower than 0.701 keV, our calculated MAC agrees well with the other experimental MACs and with the theoretical calculations, as shown in the inset in Figure 7. The calculated MAC curve is relatively noisy because, in this energy range, the X-ray intensity is coming from the very side of the tail of the Fe L$\alpha$ X-ray line. In the energy range from 0.690 to 0.701 keV, the small difference between the intensities recorded at different accelerating voltages, in addition to the high statistical noise due to the low counting rate, makes the determination of the MAC difficult and relatively variable. But by averaging the data from 0.695 to 0.700 keV, far from the $L_3$ edge, a MAC of 2,146 ± 145 $cm^2/g$ is obtained, which agrees with the other theoretical and experimental values. The data can also be fitted with a linear curve in this energy range for more precision.

At higher X-ray energies (>0.700 keV), our EPMA-derived MAC measurements are unable to reproduce the resonances (strong increases in the MAC) of the MAC visible in the two other sets of experimental data. As detailed previously, this is mainly due to the response function of the microprobe spectrometers that records the X-rays in a range of energies and not only at one single X-ray energy, convoluting the near-edge structure of the MAC with the spectrometer response function.

Consequently, as those authors sought to warn us, the Pouchou and Pichoir method of measuring the MAC is thus not valid when the MAC is changing rapidly in the vicinity of the measurement.

## Back to Castaing

Castaing, the father of EPMA, proposed in his landmark 1951 thesis (Castaing, 1951), a simple version of what we show here, an "alpha correction factor" for simple binary compounds, albeit for K$\alpha$ X-rays (which are far from the K absorption edge for most of the elements of the periodic table). This approach was developed in more practical detail a decade later by Ziebold & Ogilvie (1963) and ultimately into the Bence & Albee (1968) correction factors for geological materials.

We have shown above, in Figure 3 and Table 3, that our twist on Castaing's "alpha correction factor", in our case utilizing $k$-ratios of the integrated full wavescans of the Fe L$\alpha$ and L$\beta$ X-ray lines, generate relatively simple equations which provide marked improvements over the traditional matrix correction algorithms. In the above discussion, we have shown theoretically why this approach should work, and why the usual matrix correction (phi-rho-$Z$) should not. We also noted, significantly, that the equation generated by the data in Figure 3 should be constant for all spectrometers, with any crystal or spectrometer, on any electron beam instrument, as long as the takeoff angle is 40°. We welcome others to test our challenge.

The method originally shown by Castaing mainly consists of measuring the X-ray intensity at the maximum of the peak and on each side of the peak to subtract the background, on binary compounds of known composition and for a given experimental setup. The concentration of the element of interest A in the binary AB is then related to the $k$-ratio $k^A_{AB}$ by a function of the form:

$$\frac{1-k^A_{AB}}{k^A_{AB}} = \alpha^A_{AB}\frac{1-C^A_{AB}}{C^A_{AB}}$$

in which the only parameter (coefficient) is the $\alpha$ factor for element A in binary AB. More advanced methods were assuming that the $\alpha$ factor can be better described by a second-order polynomial that depends of the concentration $C^A_{AB}$ (Armstrong, 1988).

Expanding upon these ideas, we have measured the background subtracted X-ray intensity, at 7 kV, at the maximum of the Fe L$\alpha$ X-ray line for each sample. (Notice that due to bonding effects, the maximum of the peak was shifted from one sample to another, and therefore high-resolution peak scans were performed.) The intensities were ratioed to that of a pure Fe standard, creating a new set of Fe L$\alpha$ peak $k$-ratios, plotted against the sample Fe content. The curves obtained are very similar to the curves obtained using the area $k$-ratio method and can be reasonably fitted using a third-order polynomial function (Fig. 8).

Better results are obtained when the calibration curve is obtained by fitting the X-ray peak intensity versus the Fe concentration. However, this is not very practical as the curve returns a $k$-ratio for a given concentration. The third-order polynomial equation cannot be inverted for practical use as it has complex roots. However, the equation is simple enough to be evaluated and tabulated for a range of Fe concentrations using a spreadsheet program. The unknown $k$-ratio, and thus the corresponding

unknown Fe concentration can be found by linear interpolation of the closest *k*-ratio values found in the spreadsheet. For each spectrometer, the curves were used to re-evaluate the Fe content of our Fe–Si samples, as shown in Table 4.

For the samples containing 33.60 and 67.93 Fe wt%, the predictions of the calibration curves deviate strongly from the expected concentration, up to 5.8 Fe wt%. As it can be seen in Figure 8, the calibration curves are relatively far from the experimental data for these two samples. In addition, for the SXES using the JS2000 grating and the 4,096 channels CCD camera, the energy bin size is relatively large making the maximum of the peak truncated and adding a small error to the X-ray intensity measurement.

We know for no theoretical reason why this approach should work for the Fe L$\alpha$ peak; it is clearly inferior to the summed Fe L$\alpha$ + L$\beta$ peak scan approach shown earlier. However, this method has the advantage to be easier to use than the one involving the area *k*-ratio but, it has the disadvantage to not be universal, as explained in the theoretical section, meaning that the curve depends on the spectrometer used and it would have to be acquired for each instrument/spectrometer. It also gives a less accurate quantification number compared with the area *k*-ratio calibration curve.

## Conclusions

The evaluation of the MAC close to the absorption edges cannot be done by EPMA using the traditional method by Pouchou and Pichoir. The theory behind the ZAF or the phi-rho-*Z* methods assumes an ideal spectrometer without broadening. Close to an absorption edge, these methods fail, even with perfect atomic parameters. However, we show that it is possible to derive a universal calibration curve that can be used on any spectrometer (with a takeoff angle of 40°) for a given accelerating voltage and allows for the quantification of Fe in Fe–silicides. This method utilizes the Fe L$\alpha$ and L$\beta$ X-ray line area *k*-ratios relative to a pure Fe–metal standard. The use of this calibration curve at 7 kV shows good quantification results on our set of 10 Fe-silicide samples. An additional study using Fe L$\alpha$ peak *k*-ratios showed limited improvement over the usual matrix correction method.

An associated study of olivine crystals ($Fe_2SiO_4$–$Mg_2SiO_4$ solid solution) with Fe concentrations ranging from 8 to 53 wt% Fe has yielded a similar type calibration curve with equally good quantification results. Future work will apply this technique to other families of materials such as iron sulfides, iron oxides, and various iron-bearing silicate minerals.

**Author ORCIDs.** Aurélien Moy, 0000-0001-7020-3776.

**Acknowledgments.** The authors would like to thank the two reviewers for their detailed comments. Support for this research came from the National Science Foundation: EAR13-37156 (JHF), EAR15-54269 (JHF), and EAR-1625422 (AVDH).

## References

**Armstrong JT** (1988). Bence-Albee after 20 years: Review of the accuracy of $\alpha$-factor correction procedures for oxide and silicate minerals. In *Microbeam Analysis*, Newbury DE (Ed.), pp. 469–476. San Francisco: San Francisco Press.

**Bence AE & Albee AL** (1968). Empirical correction factors for the electron microanalysis of silicates and oxides. *J Geol* **76**(4), 382–403.

**Buse B & Kearns S** (2018). Quantification of olivine using Fe L$\alpha$ in electron probe microanalysis (EPMA). *Microsc Microanal* **24**, 1–7.

**Castaing R** (1951). Application des sondes électronique à une méthode d'analyse ponctuelle chimique et cristallographique. PhD Thesis. University of Paris, France. Publication ONERA No. 55.

**Chantler CT, Olsen K, Dragoset RA, Chang J, Kishore AR, Kotochigova SA & Zucker DS** (2005). X-ray form factor, attenuation and scattering tables (version 2.1). National Institute of Standards and Technology, Gaithersburg, MD. Available at http://physics.nist.gov/ffast (retrieved August 15, 2018).

**Chen CT, Idzerda YU, Lin H-J, Smith NV, Meigs G, Chaban E, Ho GH, Pellegrin E & Sette F** (1995). Experimental confirmation of the X-ray magnetic circular dichroism sum rules for iron and cobalt. *Phys Rev Lett* **75**, 152–155.

**Cullen DE, Hubbell JH & Kissel L** (1997). *EPDL97 The Evaluated Data Library*, Technical Report UCRL-50400. Livermore, CA: Lawrence Livermore National Laboratory.

**Donovan J, Kremser D, Fournelle J & Goemann K** (2018). *Probe for Windows User's Guide and Reference*, Enterprise edition. Eugene, OR: Probe Software, Inc.

**Elam WT, Ravel BD & Sieber JR** (2002). A new atomic database for X-ray spectroscopic calculations. *Radiat Phys Chem* **63**(2), 121–128.

**Essene EJ & Fisher DC** (1986). Lightning strike fusion: Extreme reduction and metal-silicate liquid immiscibility. *Science* **234**, 189–193.

**Fournier C, Merlet C, Dugne O & Fialin M** (1999). Standardless semi-quantitative analysis with WDS-EPMA. *J Anal At Spectrom* **14**, 381–386.

**Goldstein JI, Newbury DE, Michael JR, Ritchie NWM, Scott JHJ & Joy DC** (2018). Electron beam—specimen interactions: Interaction volume. In *Scanning Electron Microscopy and X-Ray Microanalysis*, 4th ed. pp. 1–14, New York, NY: Springer.

**Gopon P, Fournelle J, Sobol PE & Llovet X** (2013). Low-voltage electron-probe microanalysis of Fe–Si compounds using soft X-rays. *Microsc Microanal* **19**, 1698–1708.

**Heinrich KFJ** (1987). Mass absorption coefficients for electron probe microanalysis. In *Proceedings of the 11th International Congress on X-ray Optics and Microanalysis*, Brown JD & Packwood RH (Eds.), pp. 67–119. London, Ontario: University of Western Ontario Press.

**Ida T, Ando M & Toraya H** (2000). Extended pseudo-Voigt function for approximating the Voigt profile. *J Appl Cryst* **33**, 1311–1316.

**Lee JC, Xiang J, Ravel B, Kortright J & Flanagan K** (2009). Condensed matter astrophysics: A prescription for determining the species-specific composition and quantity of interstellar dust using X-rays. *Astrophys J* **702**, 970–979.

**Llovet X, Pinard PT, Heikinheimo E, Louhenkilpi S & Richter S** (2016). Electron probe microanalysis of Ni silicides using Ni-L X-ray lines. *Microsc Microanal* **22**, 1233–1243.

**McSwiggen P** (2014). Characterisation of sub-micrometre features with the FE-EPMA. *IOP Conf Ser Mater Sci Eng* **55**, 012009.

**Perepezko JH & Hebert RJ** (2002). Amorphous aluminum alloys—synthesis and stability. *JOM* **54**(3), 34–39.

**Pinard PT** (2016). *Electron probe microanalysis of carbon containing steels at a high spatial resolution*. PhD Thesis. RWTH Aachen University, Germany.

**Pouchou JL** (1996). Use of soft X-rays in microanalysis. *Mikrochim Acta* **13** (Suppl), 39–60.

**Pouchou JL & Pichoir F** (1988). Determination of mass absorption coefficients for soft X-rays by use of the electron microprobe. In *Microbeam Analysis*, Newbury DE (Ed.), pp. 319–324. San Francisco: San Francisco Press.

**Pouchou JL & Pichoir F** (1991). Quantitative analysis of homogeneous or stratified microvolumes applying the model "PAP". In *Electron Probe Quantitation*, Heirinch KFJ & Newbury DE (Eds.), pp. 223–249. New York: Plenum Press.

**Rémond G, Myklebust R, Fialin M, Nockolds C, Phillips M & Roques-Carmes C** (2002). Decomposition of wavelength dispersive X-ray spectra. *J Res Natl Inst Stand Technol* **107**, 509–529.

**Rietmeijer FJ, Nakamura T, Tsuchiyama A, Uesugi K, Nakano T & Leroux H** (2008). Origin and formation of iron silicide phases in the aerogel of the Stardust mission. *Meteorit Planet Sci* **43**(1–2), 121–134.

**Salvat F** (2015). *PENELOPE-2014: A Code System for Monte Carlo Simulation of Electron and Photon Transport*. Issy-les-Moulineaux, France: OECD/Nuclear Energy Agency. Available at http://www.nea.fr/lists/penelope.html.

**Scott VD, Love G & Reed SJB** (1995). *Quantitative Electron-Probe Microanalysis*. 2nd ed. New York: Ellis Horwood.

**Shiryaev AA, Griffin WL & Stoyanov E** (2011). Moissanite (SiC) from kimberlites: Polytypes, trace elements, inclusions and speculations on origin. *Lithos* **122**, 152–164.

**Sokaras D, Kochur AG, Müller M, Kolbe M, Beckhoff B, Mantler M, Zarkadas C & Andrianis M** (2011). Cascade L-shell soft-X-ray emission as incident X-ray photons are tuned across the 1s ionization threshold. *Phys Rev A* **83**, 052511.

**STRATAGem Version 2.6**, SAMx, 4, rue Galilée, 78280 Guyancourt, France.

**Ziebold TO & Ogilvie RE** (1963). Quantitative analysis with the electron microanalyzer. *Anal Chem* **35**(6), 621–627.